analytical chemistry

Article

Cite This: Anal. Chem. 2018, 90, 6081−6088

pubs.acs.org/ac

Simultaneous Fluorescence Visualization of Endoplasmic Reticulum Superoxide Anion and Polarity in Myocardial Cells and Tissue

Haibin Xiao, Chuanchen Wu, Ping Li,* and Bo Tang*

Collaborative Innovation Center of Functionalized Probes for Chemical Imaging in Universities of Shandong, Key Laboratory of Molecular and Nano Probes, Ministry of Education, College of Chemistry, Chemical Engineering and Materials Science, Institute of Biomedical Sciences, Shandong Normal University, Jinan 250014, People's Republic of China

Supporting Information

ABSTRACT: Diabetic cardiomyopathy (DCM) is a critical complication of diabetes, the accurate pathogenesis of which remains elusive. It is widely accepted that endoplasmic reticulum (ER) stress and abnormal fluctuations of reactive oxygen species (ROS) are considered to be closely associated with progress of DCM. In addition, DCM-induced changes of myocardial tissue and ROS-derived oxidation of proteins will cause changes of the hydrophilic and hydrophobic domains and may further seriously alter the myocardial cell polarity. Thus, real-time detection of ROS and polarity in ER of live cells and in tissue will contribute to revealing the exact molecular mechanisms of DCM. In this article, we first present an ER-targetable fluorogenic probe termed ER-NAPC for sensitive and selective detection of superoxide anion ($O_2^{\bullet-}$). ER-NAPC can precisely target ER and visualize the increase of $O_2^{\bullet-}$ level in a live H9c2 cardiomyocyte cell during ER stress. Meanwhile, by combining ER-NAPC with a polarity-sensitive probe, ER-P, we accomplish the simultaneous fluorescence visualization of $O_2^{\bullet-}$ and polarity in ER of live cells and diabetic myocardial tissue. The dual-color fluorescence imaging results indicate that the $O_2^{\bullet-}$ level and polarity will synergistically rise during ER stress in live cells and diabetic myocardial tissue. The proposed dual-color imaging strategy may offer a proven methodology for studying coordinated variation of different parameters during ER stress oriented disease.

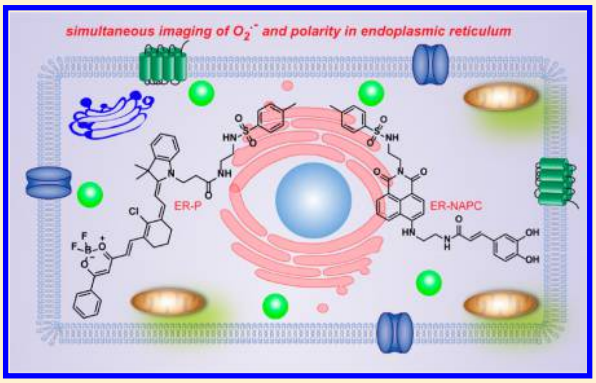

Diabetes mellitus, as a metabolic disease, leads to significant morbidity and mortality.[1] In particular, diabetic cardiomyopathy (DCM) characterized by cardiac fibrosis is a critical complication of diabetes and a leading cause of death.[2,3] The occurrence and development of DCM is a chronic and complicated process that is involved in abnormal cellular metabolism and dysfunctions in organelles, such as myofibrils, mitochondria, and sarcolemma.[4−8] Although multiple mechanisms for the progress of DCM have been proposed, including excess oxidative stress, impaired calcium homeostasis, mitochondrial dysfunction, and activation of apoptotic signaling pathways,[9−13] the accurate pathogenesis of DCM remains incompletely understood.

When normal functions of the endoplasmic reticulum (ER) were disturbed by various conditions, such as glucotoxicity, ER Ca^{2+} disequilibrium, ischemia, and hypoxia, free radicals, increased protein synthesis, and ER stress will appear accompanying production of reactive oxygen species (ROS).[14] Recently, a number of studies have demonstrated the crucial role of ER stress and increased ROS in the development of DCM.[15−17] For instance, the markers of ER stress are elevated in the hearts of diabetic animals; ROS contribute to diabetes-induced cardiomyocytes damage, and metallothionein will prevent diabetes-induced deficits in cardiomyocytes by inhibiting ROS production.[18,19] Superoxide anion ($O_2^{\bullet-}$), as the most important and first produced ROS, is the precursor of other ROS. The concentration variations of $O_2^{\bullet-}$ determine the level of other ROS.[20] In addition, on the one hand, DCM will result in many changes in the microstructure and morphology of myocardial tissue, such as fibrosis and myocardial hypertrophy,[21] and on the other hand, the overproduction ROS will oxidize the thiolate of protein to sulfenic acid further to sulfinic acid and sulfonic acid,[22,23] which probably cause dysfunction of protein secretion and modification as well as changes of hydrophilic and hydrophobic domains, and thus might affect the ER polarity environment.[24] Therefore, developing a new method for real-time detection of $O_2^{\bullet-}$ and polarity in ER of live cells and in tissue will contribute to uncovering the exact molecular mechanisms of DCM.

Fluorescence imaging is emerging as a promising and powerful means for monitoring various bioactive molecules in living systems, which is thanks to its remarkable advantages, such as easy operation, high sensitivity, and high temporal−spatial resolution.[25−37] In particular, due to the distinguishable spectra, it can study the synergistic changes of different

Received: December 28, 2017
Accepted: April 17, 2018
Published: April 17, 2018

DOI: 10.1021/acs.analchem.7b05440
Anal. Chem. 2018, 90, 6081−6088

Scheme 1. (a) Structure of ER-NAPC and the Proposed Sensing Mechanism for $O_2^{\bullet-}$ and (b) Schematic Diagram of Simultaneous Fluorescence Visualization of $O_2^{\bullet-}$ and Polarity in ER

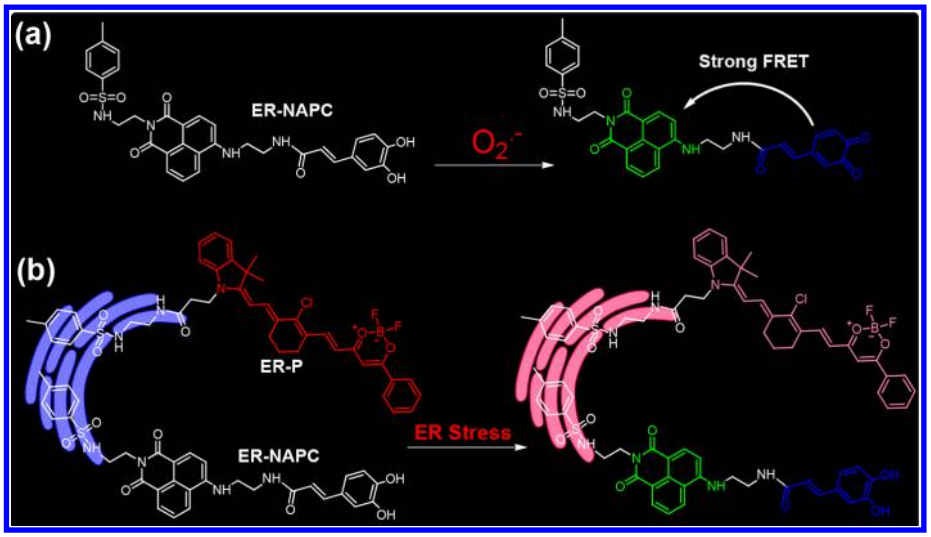

bioactive species through simultaneous fluorescence detection. However, up to now, although many representative organelle-targetable $O_2^{\bullet-}$ and polarity-responsive fluorescent probes have been presented,[38−45] and simultaneous monitoring of multiple species was also reported,[46−50] specific sensors suitable for visualization of ER $O_2^{\bullet-}$ and further simultaneous fluorescence imaging of ER $O_2^{\bullet-}$ and polarity in live cells and tissues have not been explored.

To solve the above-mentioned problem, it is an urgent need to develop a new method for simultaneous fluorescence imaging of ER $O_2^{\bullet-}$ and polarity. In the previous work, we have successfully fabricated an ER-targetable near-infrared fluorescent probe, ER-P, for detection of polarity.[44] ER-P consists of a merocyanine moiety containing a tertiary amine as electron donor and a difluoroboronate moiety as electron acceptor. Due to the intramolecular charge transfer (ICT), the fluorescence intensity of ER-P at 800 nm decreases seriously along with increasing polarity of the media, which can indicate the polarity. Synchronously, to achieve the imaging of $O_2^{\bullet-}$ in live tissues, an ideal $O_2^{\bullet-}$-responsive fluorescent probe with instantaneous response, high fluorescence quantum yield, and long emission wavelength should be presented. Thus, we herein first developed a new ER-targetable fluorogenic probe termed ER-NAPC for detection of $O_2^{\bullet-}$. As shown in Scheme 1a, ER-NAPC consists of 1,8-naphthalimide (a potent fluorophore), caffeic acid group (the $O_2^{\bullet-}$ recognition unit), and methyl sulphonamide (ER-targetable moiety). The caffeic acid group in ER-NAPC can react with $O_2^{\bullet-}$ instantaneously and is oxidized from pyrocatechol to benzoquinone, which will result in an intense fluorescence resonance energy transfer (FRET) and emit strong fluorescence of the naphthalimide moiety. Thus, after reaction with $O_2^{\bullet-}$, ER-NAPC will exhibit obviously increased fluorescence quantum yield. In addition, the imino group and amide in ER-NAPC form the donor−acceptor system, rendering long emission wavelength, which is beneficial to tissue imaging. Because ER-NAPC and ER-P display distinguishable excitation and emission spectra (405/545 nm for ER-NAPC and 633/800 nm for ER-P), we achieved the simultaneous fluorescence visualization of $O_2^{\bullet-}$ and polarity during ER stress by utilizing ER-NAPC and ER-P with a spectral distinguishable imaging method (Scheme 1b). Furthermore, this dual-color imaging method was utilized for simultaneous fluorescence imaging of $O_2^{\bullet-}$ and polarity in normal and diabetic myocardial tissues.

EXPERIMENTAL SECTION

Materials and General Methods. Unless otherwise stated, all reagents were purchased from commercial suppliers and used without further purification. The solvents were purified by conventional methods before use. ER-Tracker Red was purchased from Invitrogen (U.S.A.). 3-(4,5-Dimethylthiazol-2-yl)-2,5-diphenyl tetrazolium bromide (MTT), tunicamycin (Tm), thapsigargin (Tg), and streptozotocin (STZ) were purchased from Sigma. 4-Hydroxy-2,2,6,6-tetramethylpiperidine-*N*-oxyl (TEMPO) was purchased from J&K Chemical. Superoxide dismutase (SOD) was purchased from Solarbio. Silica gel (200−300 mesh) used for flash column chromatography was purchased from Qingdao Haiyang Chemical Co., Ltd. ^{1}H NMR and ^{13}C NMR spectra were determined by 300 MHz and 75 (or 100) MHz using Bruker NMR spectrometers. The mass spectra were obtained by a Bruker Maxis ultrahigh-resolution time-of-flight mass spectrometry (TOF MS) system. The fluorescence spectra measurements were performed using an FLS-980 Edinburgh, a Hitachi F-4600, and a Varian Cary Eclipse fluorescence spectrophotometers. The adult KM mice (female, 6−8 week-old, 20 ± 2 g) were purchased from the laboratory animal center of Shandong University (Jinan, China). All animal experiments were conducted at the laboratory of Shandong Normal University in compliance with the Guidelines of Shandong Normal University for the Care and Use of Laboratory Animals. Confocal fluorescence imaging in cells and in mice was performed with a Leica TCS SP8 (one-photon) or Zeiss LSM 880 NLO (two-photon) confocal laser scanning microscope. The laser power of confocal imaging is 5.0 mW for the 405 nm laser, and 15 mW for the 561 and 633 nm laser. The two-photon excitation wavelength is 800 nm. The cardiomyocyte cells (H9c2) and human hepatoma cells (HepG2) were purchased from the Cell Bank of the Chinese Academy of Sciences (Shanghai, China).

Synthesis of Compound ER-NapNH2. Under argon atmosphere, compound ER-NapBr (474 mg, 1.0 mmol), ethylenediamine (600 mg, 10 mmol), and triethylamine (0.50

DOI: 10.1021/acs.analchem.7b05440
Anal. Chem. 2018, 90, 6081−6088

mL) were successively added to the stirred solution of 2-methoxyethanol (10 mL) in a round-bottomed flask. After heating at 100 °C for 10 h, the mixture was cooled to room temperature and poured into diethyl ether. The resulting precipitate was filtered and purified by silica gel chromatography with CH_2Cl_2/CH_3OH (5:1) as the eluent to yield ER-NapNH2 as a yellow solid (230 mg, 50%). ^{1}H NMR (300 MHz, d_6-DMSO) δ (ppm): 2.263 (s, 3H), 2.645 (s, 2H), 2.921 (t, J = 4.71 Hz, 2H), 3.027 (t, J = 5.4 Hz, 2H), 3.407 (d, J = 4.8 Hz, 2H), 4.063 (t, J = 4.8 Hz, 2H), 6.765 (d, J = 6.6 Hz, 1H), 7.240 (d, J = 6.0 Hz, 2H), 7.592−7.653 (m, 3H), 7.854 (s, 1H), 8.174 (d, J = 6.3 Hz, 1H), 8.345 (d, J = 5.4 Hz, 1H), 8.700 (d, J = 6.3 Hz, 1H). ^{13}C NMR (75 MHz, d_6-DMSO) δ (ppm): 21.3, 46.4, 58.5, 60.5, 74.4, 104.2, 108.1, 120.6, 122.2, 124.6, 126.8, 129.1, 129.9, 130.9, 134.6, 138.1, 142.9, 151.3, 163.4, 164.3. HRMS (ESI) m/z calcd for $C_{23}H_{24}N_4O_4S$ [M + H$^+$], 453.1591; found, 453.1617.

Synthesis of ER-NAPC. Under argon atmosphere, caffeic acid (180 mg, 1.0 mmol), *N*-hydroxybenzotrizole (HOBT, 135 mg, 1.0 mmol), and 1-ethyl-3-(3-dimethylaminopropyl) carbodiimide hydrochloride (EDC, 192 mg, 1.0 mmol) were dissolved in 2.0 mL of dimethylformamide (DMF) and 8.0 mL of dichloromethane. The mixture was stirred at 0 °C for 30 min, and then compound ER-NapNH2 (452 mg, 1.0 mmol) dissolved in 2.0 mL of dimethylformamide was added to the mixture. All the solution reacted at 25 °C for 24 h. The resulting mixture was concentrated and purified by silica gel chromatography with CH_2Cl_2/CH_3OH (10:1) as the eluent to yield ER-NAPC as a yellow solid (250 mg, 40%). ^{1}H NMR (300 MHz, d_6-DMSO) δ (ppm): 1.608−1.678 (m, 2H), 1.970−2.032 (m, 2H), 2.262 (s, 3H), 3.031−3.044 (m, 2H), 4.079 (t, J = 5.1 Hz, 2H), 5.321 (s, 1H), 6.294 (d, J = 12 Hz, 1H), 6.367 (d, J = 12 Hz, 1H), 6.776 (d, J = 6.0 Hz, 1H), 6.846−6.893 (m, 2H), 7.061 (s, 1H), 7.237 (d, J = 6.0 Hz, 2H), 7.330 (d, J = 12 Hz, 1H), 7.506 (d, J = 12 Hz, 2H), 7.606 (d, J = 6.0 Hz, 2H), 8.248 (d, J = 6.0 Hz, 1H), 8.411 (d, J = 5.4 Hz, 1H), 8.651 (d, J = 6.0 Hz, 1H), 9.169 (s, 2H). ^{13}C NMR (100 MHz, d_6-DMSO) δ (ppm): 21.34, 29.50, 29.54, 37.97, 43.41, 104.15, 108.36, 114.32, 116.22, 118.54, 120.56, 121.02, 122.36, 124.80, 126.71, 126.84, 128.00, 128.23, 128.85, 129.92, 130.11, 131.11, 134.61, 138.03, 140.06, 142.89, 146.01, 147.90, 151.00, 163.39, 164.28, 166.83. HRMS (ESI) m/z calcd for $C_{32}H_{30}N_4O_7S$ [M − H$^-$], 613.1751; found, 613.1672.

Preparation of ROS and Other Active Species. $O_2^{\bullet-}$ was prepared by dissolving KO_2 in DMSO solution. The concentration of $O_2^{\bullet-}$ was determined by various concentrations of KO_2; *tert*-butyl hydroperoxide (TBHP) was delivered from 5.0% aqueous solutions; NaOCl solution was diluted appropriately in 0.1 M NaOH(aq). The concentration of OCl^- was determined based on the molar extinction coefficient at 292 nm (350 M^{-1} cm^{-1}); hydrogen peroxide (H_2O_2) was diluted appropriately in water. The concentration of H_2O_2 was determined based on the molar extinction coefficient at 240 nm (43.6 M^{-1} cm^{-1}); hydroxyl radical ($^\bullet$OH) was produced by Fenton reaction (Fe^{2+}/H_2O_2 = 1:10), and the concentration of $^\bullet$OH was equal to the Fe(II) concentration; $^1O_2$ was generated by the addition of NaOCl and H_2O_2; peroxynitrite ($ONOO^-$) was chemically provided by H_2O_2 and $NaNO_2$. The concentration of $ONOO^-$ was estimated by using an extinction coefficient of 1670 M^{-1} cm^{-1} (302 nm); The solutions of metal ions were prepared from chlorizated salts which were dissolved in deionized water.

Determination of the Detection Limit. The detection limit was calculation based on the fluorescence titration of ER-NAPC in the presence of $O_2^{\bullet-}$. The fluorescence intensity of ER-NAPC was measured by three times, and standard deviation of the blank measurement was achieved. The detection limit was calculated by the following equation: detection limit = $3\sigma/k$, where σ is the standard deviation of the blank measurement and k is the slope between the fluorescence emission intensity (I_{545} nm) versus different $O_2^{\bullet-}$ concentrations.

Determination of the Relative Fluorescence Quantum Yield. The parameter was obtained according to a previous report.[51]

Cell Incubation and Mice Culture. HepG2 and H9c2 cells were cultured in Dulbecco's modified Eagle's medium (DMEM, Invitrogen) supplemented with 10% fetal bovine serum (Invitrogen), 1.0% penicillin, and 1.0% streptomycin. The cells were seeded in confocal culture dishes, and then incubated for 24 h at 37 °C under a humidified atmosphere containing 5.0% CO_2.

The Kunming mice were intraperitoneally (ip) injected with STZ freshly dissolved in 0.01 mol/L citrate buffer (pH 4.5) at a dose of 150 mg/kg body weight after overnight fasting. At 72 h after STZ injection, the blood glucose level of mice was detected with portable glucose meter (Roche Diagnostics Corporation). The diabetes of mouse was confirmed by the presence of hyperglycemia (blood glucose level ≥16.7 mmol/L). Since then, the mice were divided into three groups: a control group, a diabetic group (oral administration of PBS), and a treated diabetic group (oral administration of metformin, 150 mg/kg twice a day). After 10 days, all the mice were ip injected with ER-NAPC (10 μM, 100 μL) and ER-P (50 μM, 100 μL) for 40 min. For the scavenging experiment, the diabetic mice were ip injected with TEMPO (10 mM, 200 μL) before the probes were loaded. Then, the mice were anesthetized with chloral hydrate (ip, 400 mg/kg). Subsequently, mice were sacrificed to surgically harvest the hearts that were immediately placed in ice-cold PBS buffer. Then, the myocardial tissue was directly imaged with two-photon confocal laser scanning microscopy with an 800 nm laser (for ER-NAPC) and one-photon 633 nm laser (for ER-P) simultaneously.

Procedure for Fluorescence Measurement. ER-NAPC was dissolved in dimethyl sulfoxide (DMSO) to produce a stock solution (0.1 mM). The solutions was diluted in PBS buffer (5.0 mM, pH 7.4, containing 10% DMSO) to the lowest concentration of 1.0 μM. The molar extinction coefficient ε was calculated according to the Beer−Lambert's law equation $A = \varepsilon bc$, where A is absorbance, b is the absorption path length (1.0 cm), and c is the concentration. Different concentrations of $O_2^{\bullet-}$ or appropriate amounts of biologically relevant analytes were added to separate portions of the solution and mixed thoroughly with 1.0 μM ER-NAPC. An FLS-980 Edinburgh fluorescence spectrometer was used to acquire the fluorescence spectra. The slit width was set to 3.0 nm. For the fluorescence stability assays, fluorescence intensity at 545 nm was collected in Varian Cary Eclipse fluorescence spectrophotometer immediately upon addition of 10 μM of $O_2^{\bullet-}$ to a solution of ER-NAPC (1.0 μM). A Hitachi F-4600 fluorescence spectrophotometer was used to detect the fluorescence response of ER-NAPC to $O_2^{\bullet-}$ at different pH values.

DOI: 10.1021/acs.analchem.7b05440
Anal. Chem. 2018, 90, 6081−6088

RESULTS AND DISCUSSION

Synthesis of Probe ER-NAPC. The new ER-targetable $O_2^{\bullet-}$-responsive fluorogenic probe ER-NAPC was readily synthesized in two steps as illustrated in Scheme S1. ER-NapBr has been synthesized and reported by our previous work.[52] Reaction of compound ER-NapBr and ethylenediamine produced ER-NapNH2. ER-NAPC was obtained from ER-NapNH2 via a typical amidation reaction with caffeic acid in anhydrous DMF and CH_2Cl_2. The final structures of ER-NapNH2 and ER-NAPC were well-characterized with ^1H NMR, ^{13}C NMR, and high-resolution mass spectrometry (HRMS).

Spectral Response of Probe ER-NAPC to $O_2^{\bullet-}$. We first test whether ER-NAPC can respond to $O_2^{\bullet-}$ under physiological condition (pH 7.4, 5.0 mM PBS) by evaluating the absorption and fluorescence of ER-NAPC in the presence or absence of $O_2^{\bullet-}$. As shown in Figure 1a, the probe ER-NAPC has two absorption maxima at about 327 nm ($\varepsilon = 6.4 \times 10^4$ M^{-1} cm^{-1}) and 460 nm ($\varepsilon = 4.8 \times 10^4$ M^{-1} cm^{-1}), which should be assigned to caffeic acid and naphthalimide moieties, respectively. After being reacted with $O_2^{\bullet-}$, the absorption maxima at these two wavelengths displayed slight increase. Concomitantly, compared with the ER-NAPC alone, a significantly enhanced fluorescence signal at 545 nm (Figure 1b) appeared upon addition of $O_2^{\bullet-}$ because the caffeic acid was instantaneously oxidized to benzoquinone and intense FRET occurred, thereby demonstrating that ER-NAPC is a very sensitive $O_2^{\bullet-}$-responsive probe. Meanwhile, when $O_2^{\bullet-}$ was first scavenged with the universal free-radical scavenger TEMPO (10 mM), the fluorescence enhancement of ER-NAPC was almost abolished. Furthermore, ER-NAPC showed obvious turn-on fluorescence response to the xanthine/xanthine oxidase (XA/XO) system that is another source of $O_2^{\bullet-}$, and the fluorescence was also inhibited once XA/XO was pretreated with SOD (Figure S1). Then, we investigated the fluorescence response ability of ER-NAPC to different concentrations of $O_2^{\bullet-}$ under physiological condition in detail.

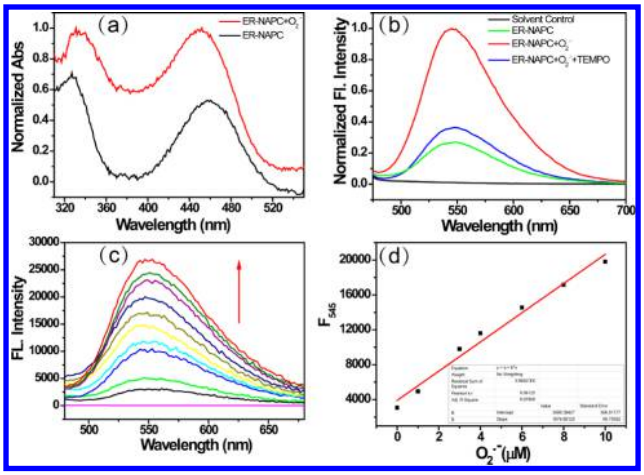

Figure 1. Spectral response of ER-NAPC to $O_2^{\bullet-}$ in PBS (pH 7.4, 5.0 mM, 10% DMSO). (a) The normalized absorption spectra of ER-NAPC (1.0 μM) in the absence or presence of $O_2^{\bullet-}$ (10 μM). (b) The normalized fluorescence spectra of solvent or ER-NAPC (1.0 μM) under different conditions. (c) The fluorescence spectra of ER-NAPC (1.0 μM) in the presence of different concentrations of $O_2^{\bullet-}$ (0–25 μM). (d) The linear relationship of fluorescence intensity at 545 nm and $O_2^{\bullet-}$ (0–10 μM). Ex = 400 nm.

As shown in Figure 1c, with the rise of $O_2^{\bullet-}$, the fluorescence spectra of ER-NAPC enhanced dramatically, and the fluorescence intensity at 545 nm increased gradually (Figure S2). The fluorescence intensity of ER-NAPC at 545 nm fits linear relationship equation $F = 1674.85[O_2^{\bullet-}] + 3906.39$ with $O_2^{\bullet-}$ concentration at 0–10 μM with a detection limit of 130 nM (Figure 1d), demonstrating that ER-NAPC can detect the $O_2^{\bullet-}$ in live cells,[20,53−55] and the relative fluorescence quantum yield increased from 0.06 to 0.39 in the absence and presence of $O_2^{\bullet-}$. The above data verified that our design strategy effectively improved the sensitivity of ER-NAPC because of the increase in fluorescence quantum yield. Upon reaction with $O_2^{\bullet-}$, ER-NAPC displayed a relative long emission wavelength at 545 nm, which is prone to tissue imaging. These results indicated ER-NAPC is highly sensitive to $O_2^{\bullet-}$ and possesses potential ability for quantitative determination of $O_2^{\bullet-}$ concentrations in a large range.

Selectivity and Stability of ER-NAPC to $O_2^{\bullet-}$. Next, The selectivity of probe ER-NAPC for $O_2^{\bullet-}$ over other potential interfering agents under biological conditions was investigated by fluorescence spectroscopy. We detected the fluorescence spectra of ER-NAPC in the presence of various ROS and metal ions. After addition of these analytes, the fluorescence of ER-NAPC showed almost no changes compared to that of ER-NAPC alone. In sharp contrast, the fluorescence of ER-NAPC exhibited significant enhancement after addition of $O_2^{\bullet-}$ (Figure 2, parts a and b). In addition, Figure S3 demonstrated

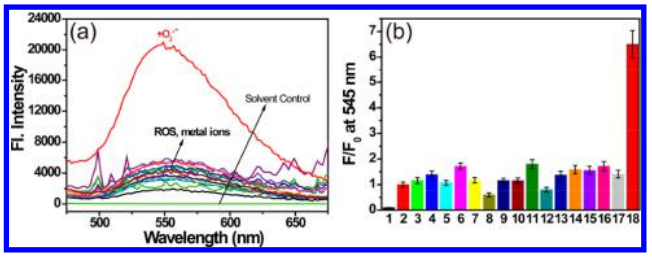

Figure 2. Fluorescence response of ER-NAPC to various interfering species in PBS (pH 7.4, 5.0 mM, 10% DMSO). (a) The fluorescence spectra of ER-NAPC (1.0 μM) with various analytes. (b) The fluorescence intensity ratios (F/F_0) of ER-NAPC at 545 nm for various analytes. F_0 indicates the blank fluorescence of ER-NAPC alone, and F represents the fluorescence of ER-NAPC in the presence of corresponding analytes. 1: Solvent control. 2: Probe blank. 3: H_2O_2, 10 mM. 4: OCl^-, 100 μM. 5: TBHP, 100 μM. 6: $ONOO^-$, 100 μM. 7: $^1O_2$, 100 μM. 8: $^{\bullet}OH$, 100 μM. 9: Na^+, 10 mM. 10: K^+, 10 mM. 11: Zn^{2+}, 0.5 mM. 12: Cu^{2+}, 100 μM. 13: Fe^{3+}, 100 μM. 14: Al^{3+}, 100 μM. 15: Mn^{2+}, 100 μM. 16: Ca^{2+}, 0.5 mM. 17: Mg^{2+}, 0.5 mM. 18: $O_2^{\bullet-}$, 10 μM. Ex = 400 nm.

that ER-NAPC can well respond to $O_2^{\bullet-}$ under wide physiological conditions (pH 6.0–8.0). Furthermore, the probe ER-NAPC alone and the reaction product of ER-NAPC with $O_2^{\bullet-}$ were stable (Figure S4). Therefore, all these data demonstrated that ER-NAPC displayed excellent selectivity for $O_2^{\bullet-}$ over other species and had favorable pH stability and photostability, which may be powerful for detection of $O_2^{\bullet-}$ in a complex biological system.

Fluorescence Imaging of $O_2^{\bullet-}$ in Live Cells with ER-NAPC. With this excellent probe in hand, we next intended to test the application of ER-NAPC in live cells fluorescence imaging. First, we performed standard MTT assays to evaluate the cytotoxicity of ER-NAPC in live cells. The data in Figure S5 showed that ER-NAPC exhibits very low cytotoxicity. To start,

DOI: 10.1021/acs.analchem.7b05440
Anal. Chem. 2018, 90, 6081−6088

H9c2 cardiomyocyte cells were incubated with high glucose (25 mM) for 24 h, which is widely considered to induce production of ROS and ER stress.[56] After being incubated with ER-NAPC, the H9c2 cells were imaged with the confocal fluorescence microscope. Obviously, these H9c2 cells emitted bright green fluorescence, indicating the production of $O_2^{\bullet-}$, and the green fluorescence vanished when the cells pretreated with TEMPO or SOD (Figure S6), verifying the specificity of ER-NAPC to $O_2^{\bullet-}$. Moreover, the photostability of ER-NAPC had been investigated in live H9c2 cells, as shown in Figure S7. The fluorescence intensity of ER-NAPC showed just 10% reduction under 5 min of continuous irradiation, suggesting that the probe had excellent photostability and leakage did not occur during experimentation. Additionally, the high glucose stimulated H9c2 cells were incubated with ER-NAPC and ER-Tracker Red (a commercial ER dye) for a colocalization experiment. As shown in Figure 3, the results suggested that the

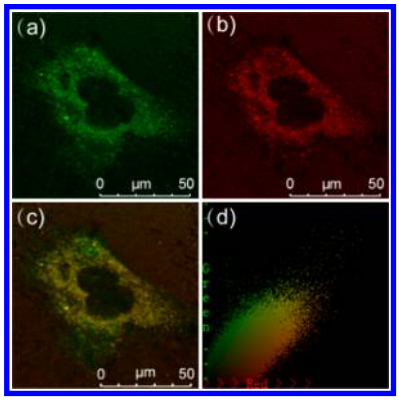

Figure 3. Colocalization fluorescence images of H9c2 cells stained with ER-NAPC and ER-Tracker Red after being induced with high glucose. (a) The fluorescence image from ER-NAPC (1.0 μM, Ex = 405 nm, collected at 450−600 nm). (b) The fluorescence image from ER-Tracker Red (500 nM, Ex = 561 nm, collected at 580−630 nm). (c) The overlay image of panels a and b. (d) Intensity correlation plot of stain ER-NAPC and ER-Tracker Red. Scale bar: 50 μm.

green fluorescence of ER-NAPC overlapped well with the red fluorescence of ER-Tracker Red (Figure 3c), with a high colocalization coefficient of 0.92. Further colocalization experiments implied that ER-NAPC rarely entered into the mitochondria, lysosomes, and Golgi apparatus of H9c2 cells and can also accumulate into ER of HepG2 cells (Figures S8 and S9). All the above data illustrated that ER-NAPC is membrane-permeable and can solely accumulate into ER to detect $O_2^{\bullet-}$ in live cells.

When cells undergo ER stress, ROS will be produced, and the generated ROS signaling will contribute to aggravating oxidative stress and cause further ER stress, which will form a vicious cycle and underlie many ER stress-associated diseases.[57] To further explore the bioapplication of ER-NAPC, we want to utilize ER-NAPC to track the production of endogenous $O_2^{\bullet-}$ under ER stress. After being incubated with ER-NAPC (1.0 μM) for 30 min, H9c2 cells were stimulated with tunicamycin (Tm, 5.0 μg/mL), which is an inhibitor of protein N-glycosylation and can trigger ER stress.[58] The time-dependent fluorescence images of H9c2 cells are exhibited in Figure 4a. It shows that the fluorescence intensity of ER-NAPC rises obviously (Figure 4b), indicating the production of $O_2^{\bullet-}$ within ER accompanying ER stress. Similarly, the level of $O_2^{\bullet-}$ will increase (Figure S10) after treatment with thapsigargin (Tg), an inhibitor of the ubiquitous ER Ca^{2+}-ATPases in mammalian cells, which can also cause ER stress.[59] A further experiment was performed by adding Tm to HepG2 cells, displaying the gradual rise of $O_2^{\bullet-}$ concentration (Figure S11). The data manifested that, during ER stress, $O_2^{\bullet-}$ can be generated. The level fluctuations of $O_2^{\bullet-}$ under such conditions can be monitored by ER-NAPC, which confirmed that ER-NAPC is capable of real-time imaging of endogenous $O_2^{\bullet-}$ in living cells.

Simultaneous Fluorescence Imaging of $O_2^{\bullet-}$ and Polarity in Live Cells with ER-NAPC and ER-P. Except for production of ROS and oxidative stress, ER stress will cause dysfunction of protein secretion and modification, and ROS-derived oxidation of proteins might cause changes of the hydrophilic and hydrophobic domains, thus presumably affecting the ER polarity environment. To further visualize the fluctuation of endogenous $O_2^{\bullet-}$ and change of polarity in real time, we combined ER-NAPC with a polarity-sensitive fluorescent probe ER-P[44] for simultaneous fluorescence imaging in H9c2 cells stimulated with Tm. As expected, during incubation with Tm (5.0 μg/mL) within 70 min, H9c2 cells stained with ER-NAPC displayed a successive increment of the green fluorescence (Figure 5, green channel), indicating the rise of endogenous $O_2^{\bullet-}$ contents within ER. Meanwhile, ER-P exhibited reduced red fluorescence (Figure 5, red channel), which implied the increase of polarity in ER. Further experiments in HepG2 cells obtained the same results that $O_2^{\bullet-}$ level and polarity will synergistically rise during ER stress induce by Tm (Figure S12). All these data confirmed the synergistic effect of endogenous $O_2^{\bullet-}$ and polarity. By utilizing

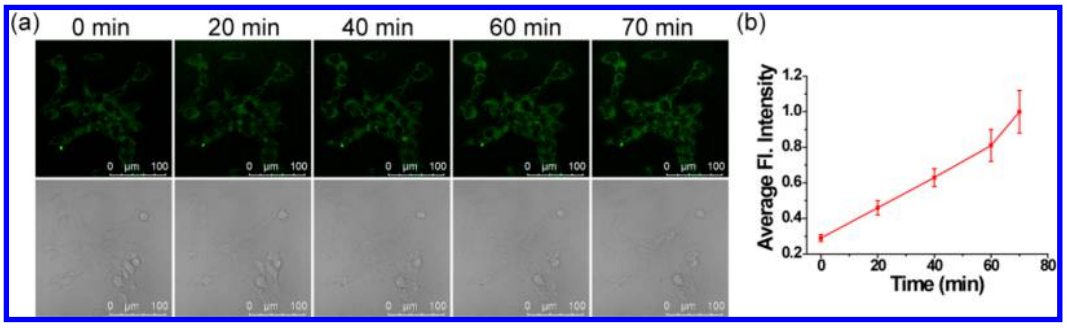

Figure 4. (a) The time-dependent fluorescence imaging of H9c2 cells incubated with ER-NAPC during ER stress. (b) The output of normalized average fluorescence intensity from panel a. The fluorescence images of H9c2 cells incubated with ER-NAPC (1.0 μM) for 30 min, and then treated with 5.0 μg/mL Tm. Ex = 405 nm, Em = 450−600 nm. Scale bar: 100 μm.

DOI: 10.1021/acs.analchem.7b05440
Anal. Chem. 2018, 90, 6081−6088

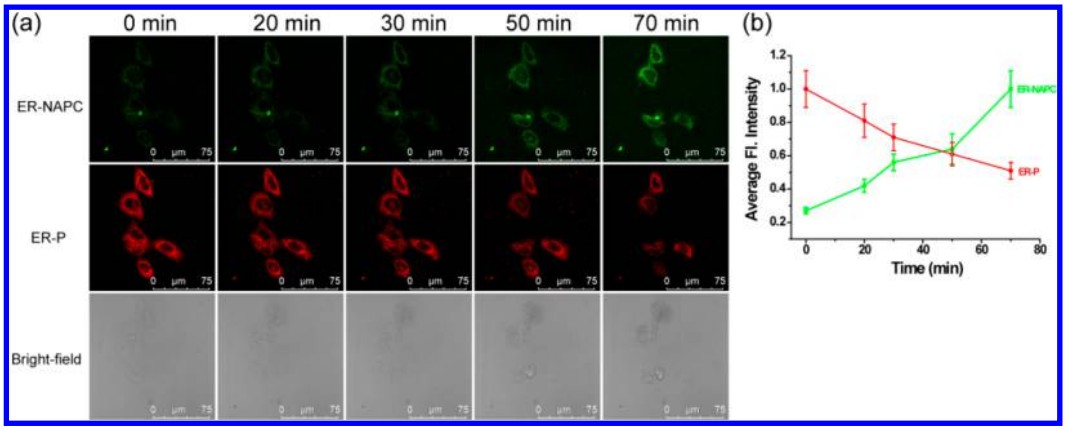

Figure 5. (a) Confocal fluorescence images of H9c2 cells stained simultaneously with ER-NAPC (1.0 μM) and ER-P (5.0 μM) in the presence of Tm (5.0 μg/mL) at different times. The first row (green channel) is fluorescence images for ER-NAPC collected at 450−600 nm by the excitation at 405 nm. The second row (red channel) is fluorescence images for ER-P collected at 700−800 nm by the excitation at 633 nm. The third row is bright-field images. Scale bar: 75 μm. (b) The output of normalized average fluorescence intensity from panel a.

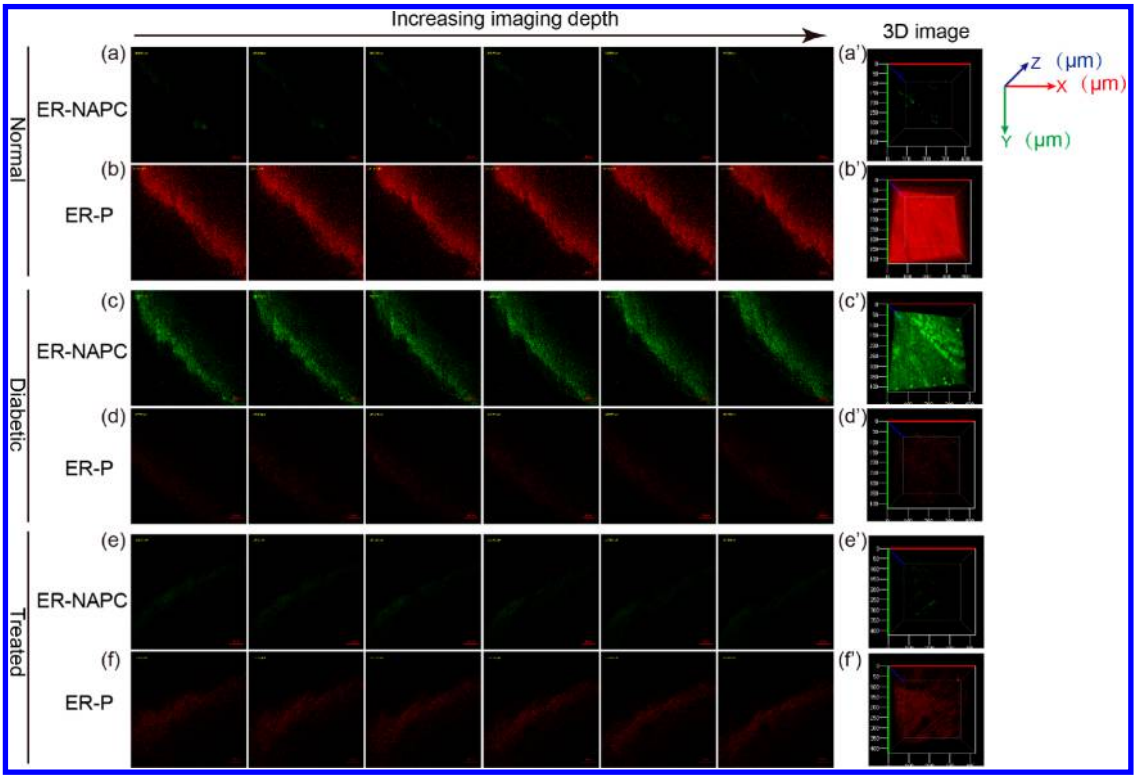

Figure 6. Confocal fluorescence imaging of endogenous $O_2^{\bullet-}$ and polarity in myocardial tissues. The green channel represents the two-photon fluorescence images from ER-NAPC (10 μM, Ex = 800, collected at 500−600 nm). The red channel represents the one-photon fluorescence images from ER-P (50 μM, Ex = 633, collected at 700−750 nm). (a and b) The selected fluorescence images of normal myocardial tissue. (c and d) The selected fluorescence images of diabetic myocardial tissue. (e and f) The selected fluorescence images of Metf-treated diabetic myocardial tissue. (a′−f′) The 3D stack images of corresponding myocardial tissue. Scale bar: 50 μm.

ER-NAPC and ER-P, we achieved the simultaneous fluorescence imaging of these two parameters.

Simultaneous Fluorescence Imaging of $O_2^{\bullet-}$ and Polarity in Myocardial Tissues with ER-NAPC and ER-P. Previous work reported that the myocardial superoxide level will be overproduced;[19] however, it is still elusive whether polarity will change. Having established the ability of ER-NAPC and ER-P to detect $O_2^{\bullet-}$ and polarity in the live cells simultaneously, we next investigated their capabilities to determinate $O_2^{\bullet-}$ and polarity in STZ-induced diabetic myocardial tissues.[60] Considering that the fluorophore 1,8-naphthalimide in ER-NAPC is an ideal two-photon dye,[61,62] we therefore took advantage of a two-photon microscope for ER-NAPC. The fluorescence images at different depths in Figure 6 demonstrate that normal myocardial tissue displayed faint green fluorescence from ER-NAPC and high red fluorescence from ER-P (Figure 6, parts a and b), implying the low concentration of $O_2^{\bullet-}$ and low-polarity environment. However, in diabetic myocardial tissue, ER-NAPC showed dramatically elevated fluorescence (Figure 6c), which illustrated that $O_2^{\bullet-}$ is overproduced. Meanwhile, ER-P emitted weak fluorescence (Figure 6d), suggesting the increase of polarity. Additionally,

DOI: 10.1021/acs.analchem.7b05440
Anal. Chem. 2018, 90, 6081−6088

when the diabetic mice were orally treated with metformin (Metf), which is a biguanide derivate used as an oral hypoglycemic drug in diabetics that has protective effects on streptozotocin-diabetic rats,[1] the $O_2^{\bullet-}$ level is reduced and the polarity decreased to some extent (Figure 6e, parts and f). These data prompted that $O_2^{\bullet-}$ level and polarity will increased in heart tissue of mice with DCM and the hypoglycemic drug Metf can partly recover the level of $O_2^{\bullet-}$ and polarity. Additionally, we also tested the selectivity of ER-NAPC to $O_2^{\bullet-}$ in diabetic myocardial tissue. As shown in Figure S13, after being preincubated with TEMPO, diabetic myocardial tissue exhibited faint fluorescence, manifesting the decrease of $O_2^{\bullet-}$. Taken together, these data indicated that ER-NAPC and ER-P can simultaneously and solely visualize $O_2^{\bullet-}$ and polarity, respectively, in myocardial tissues of normal and diabetic mice.

CONCLUSIONS

In conclusion, we have developed a new method for simultaneous fluorescence visualization of ER $O_2^{\bullet-}$ and polarity in myocardial cells and tissues. This method used a new ER-targetable fluorogenic probe termed ER-NAPC for sensitive and selective imaging of $O_2^{\bullet-}$. Due to the distinguishable spectra of ER-NAPC and our reported polarity-responsive fluorescent probe ER-P, we accomplished the simultaneous fluorescence visualization of $O_2^{\bullet-}$ and polarity during ER stress in myocardial cells by utilizing ER-NAPC and ER-P with the spectral distinguishable imaging method. The imaging results demonstrated that $O_2^{\bullet-}$ and polarity will synergistically increase under ER stress. Furthermore, the endogenous $O_2^{\bullet-}$ concentration and polarity difference in myocardial tissues of normal and diabetic mice as well as treated diabetic mice was determined with this dual-color imaging method. It was found that elevated $O_2^{\bullet-}$ level and polarity appeared in myocardial tissue of diabetic mice. We expect that this method for simultaneous imaging of $O_2^{\bullet-}$ and polarity will help to more accurately study the occurrence and development of diabetic cardiac disease. Meanwhile, the presented dual-color imaging strategy may offer a new direction for exploring the synergetic variation of different parameters during other diseases.

ASSOCIATED CONTENT

Supporting Information

The Supporting Information is available free of charge on the ACS Publications website at DOI: 10.1021/acs.analchem.7b05440.

Synthetic route, photophysical data, and cell data (PDF)

AUTHOR INFORMATION

Corresponding Authors

*E-mail: lip@sdnu.edu.cn. Phone: +86 531 86180010.
*E-mail: tangb@sdnu.edu.cn. Phone: +86 531 86180010.

ORCID

Bo Tang: 0000-0002-8712-7025

Notes

The authors declare no competing financial interest.

ACKNOWLEDGMENTS

This work was supported by the National Natural Science Foundation of China (21535004, 91753111, 21390411, 21675105, 21475079), the National Major Scientific and Technological Special Project for "Significant New Drugs Development" (2017ZX09301030004), and the Natural Science Foundation of Shandong Province of China (ZR2017ZC0225).

REFERENCES

(1) Yanardag, R.; Ozsoy-Sacan, O.; Bolkent, S.; Orak, H.; Karabulut-Bulan, O. *Hum. Exp. Toxicol.* **2005**, *24*, 129−135.
(2) Cai, L.; Kang, Y. J. *Cardiovasc. Toxicol.* **2001**, *1*, 181−193.
(3) Boudina, S.; Abel, E. D. *Circulation* **2007**, *115*, 3213−3223.
(4) Dyntar, D.; Sergeev, P.; Klisic, J.; Ambühl, P.; Schaub, M. C.; Donath, M. Y. *J. Clin. Endocrinol. Metab.* **2006**, *91*, 1961−1967.
(5) Feuvray, D. *Arch. Mal. Coeur Vaiss.* **2004**, *97*, 261−265.
(6) Tappia, P. S.; Asemu, G.; Aroutiounova, N.; Dhalla, N. S. *Mol. Cell. Biochem.* **2004**, *261*, 193−199.
(7) Ligeti, L.; Szenczi, O.; Prestia, C. M.; Szabó, C.; Horváth, K.; Marcsek, Z. L.; Van Stiphout, R.; Van Riel, N.; Den Buijs, J.; Van der Vusse, G.; Ivanics, T. *Int. J. Mol. Med.* **2006**, *17*, 1035−1043.
(8) Pereira, L.; Matthes, J.; Schuster, I.; Valdivia, H. H.; Herzig, S.; Richard, S.; Gómez, A. M. *Diabetes* **2006**, *55*, 608−615.
(9) Croston, T. L.; Thapa, D.; Holden, A. A.; Tveter, K. J.; Lewis, S. E.; Shepherd, D. L.; Nichols, C. E.; Long, D. M.; Olfert, I. M.; Jagannathan, R.; Hollander, J. M. *Am. J. Physiol-Heart. C* **2014**, *307*, H54−H65.
(10) Monji, A.; Mitsui, T.; Bando, Y. K.; Aoyama, M.; Shigeta, T.; Murohara, T. *Am. J. Physiol-Heart. C* **2013**, *305*, H295−H304.
(11) Beaudoin, M. S.; Perry, C. G. R.; Arkell, A. M.; Chabowski, A.; Simpson, J. A.; Wright, D. C.; Holloway, G. P. *J. Physiol.* **2014**, *592*, 2519−2533.
(12) Pan, Y.; Wang, Y.; Zhao, Y.; Peng, K.; Li, W.; Wang, Y.; Zhang, J.; Zhou, S.; Liu, Q.; Li, X.; Cai, L.; Liang, G. *Diabetes* **2014**, *63*, 3497−3511.
(13) Stølen, T. O.; Høydal, M. A.; Kemi, O. J.; Catalucci, D.; Ceci, M.; Aasum, E.; Larsen, T.; Rolim, N.; Condorelli, G.; Smith, G. L.; Wisløff, U. *Circ. Res.* **2009**, *105*, 527−536.
(14) Parmar, V. M.; Schroder, M. *Adv. Exp. Med. Biol.* **2012**, *738*, 153−168.
(15) Li, Z.; Zhang, T.; Dai, H.; Liu, G.; Wang, H.; Sun, Y.; Zhang, Y.; Ge, Z. *J. Clin. Biochem. Nutr.* **2007**, *41*, 58−67.
(16) Lakshmanan, A. P.; Harima, M.; Suzuki, K.; Soetikno, V.; Nagata, M.; Nakamura, T.; Takahashi, T.; Sone, H.; Kawachi, H.; Watanabe, K. *Int. J. Biochem. Cell Biol.* **2013**, *45*, 438−447.
(17) Li, Z.; Zhang, T.; Dai, H.; Liu, G.; Wang, H.; Sun, Y.; Zhang, Y.; Ge, Z. *J. Endocrinol.* **2008**, *196*, 565−572.
(18) Ye, G.; Metreveli, N. S.; Ren, J.; Epstein, P. N. *Diabetes* **2003**, *52*, 777−783.
(19) Cai, L.; Wang, J.; Li, Y.; Sun, X.; Wang, L.; Zhou, Z.; Kang, Y. J. *Diabetes* **2005**, *54*, 1829−1837.
(20) Turrens, J. F. *J. Physiol.* **2003**, *552*, 335−344.
(21) Li, J.; Zhu, H.; Shen, E.; Wan, L.; Arnold, J. M. O.; Peng, T. *Diabetes* **2010**, *59*, 2033−2042.
(22) Ray, P. D.; Huang, B. W.; Tsuji, Y. *Cell. Signalling* **2012**, *24*, 981−990.
(23) Holmström, K. M.; Finkel, T. *Nat. Rev. Mol. Cell Biol.* **2014**, *15*, 411−421.
(24) Rodriguez-Boulan, E.; Macara, I. G. *Nat. Rev. Mol. Cell Biol.* **2014**, *15*, 225−242.
(25) Frangioni, J. V. *Curr. Opin. Chem. Biol.* **2003**, *7*, 626−634.
(26) Rao, J.; Dragulescu-Andrasi, A.; Yao, H. *Curr. Opin. Biotechnol.* **2007**, *18*, 17−25.
(27) Dickinson, B. C.; Srikun, D.; Chang, C. J. *Curr. Opin. Chem. Biol.* **2010**, *14*, 50−56.
(28) Xu, Z.; Xu, L. *Chem. Commun.* **2016**, *52*, 1094−1119.
(29) Chen, X.; Wang, F.; Hyun, J. Y.; Wei, T.; Qiang, J.; Ren, X.; Shin, I.; Yoon, J. *Chem. Soc. Rev.* **2016**, *45*, 2976−3016.
(30) Vendrell, M.; Zhai, D.; Er, J. C.; Chang, Y. *Chem. Rev.* **2012**, *112*, 4391−4420.
(31) Yuan, L.; Lin, W.; Zheng, K.; He, L.; Huang, W. *Chem. Soc. Rev.* **2013**, *42*, 622−661.

DOI: 10.1021/acs.analchem.7b05440
Anal. Chem. 2018, 90, 6081−6088

(32) Tang, Y.; Lee, D.; Wang, J.; Li, G.; Yu, J.; Lin, W.; Yoon, J. *Chem. Soc. Rev.* **2015**, *44*, 5003−5015.
(33) Chen, X.; Zhou, Y.; Peng, X.; Yoon, J. *Chem. Soc. Rev.* **2010**, *39*, 2120−2135.
(34) Du, J.; Hu, M.; Fan, J.; Peng, X. *Chem. Soc. Rev.* **2012**, *41*, 4511−4535.
(35) Wang, R.; Yu, C.; Yu, F.; Chen, L.; Yu, C. *TrAC, Trends Anal. Chem.* **2010**, *29*, 1004−1013.
(36) Bull, S. D.; Davidson, M. G.; Van den Elsen, J. M. H.; Fossey, J. S.; Jenkins, A. T. A.; Jiang, Y.; Kubo, Y.; Marken, F.; Sakurai, K.; Zhao, J.; James, T. D. *Acc. Chem. Res.* **2013**, *46*, 312−326.
(37) Lee, M. H.; Kim, J. S.; Sessler, J. L. *Chem. Soc. Rev.* **2015**, *44*, 4185−4191.
(38) Hu, J. J.; Wong, N.; Ye, S.; Chen, X.; Lu, M.; Zhao, A. Q.; Guo, Y.; Ma, A. C.; Leung, A. Y.; Shen, J.; Yang, D. *J. Am. Chem. Soc.* **2015**, *137*, 6837−6843.
(39) Li, P.; Zhang, W.; Li, K.; Liu, X.; Xiao, H.; Zhang, W.; Tang, B. *Anal. Chem.* **2013**, *85*, 9877−9881.
(40) Si, F.; Liu, Y.; Yan, K.; Zhong, W. *Chem. Commun.* **2015**, *51*, 7931−7934.
(41) Xiao, H.; Liu, X.; Wu, C.; Wu, Y.; Li, P.; Guo, X.; Tang, B. *Biosens. Bioelectron.* **2017**, *91*, 449−455.
(42) Xiao, H.; Li, P.; Zhang, W.; Tang, B. *Chem. Sci.* **2016**, *7*, 1588−1593.
(43) Jiang, N.; Fan, J.; Xu, F.; Peng, X.; Mu, H.; Wang, J.; Xiong, X. *Angew. Chem., Int. Ed.* **2015**, *54*, 2510−2514.
(44) Xiao, H.; Wu, C.; Li, P.; Gao, W.; Zhang, W.; Zhang, W.; Tong, L.; Tang, B. *Chem. Sci.* **2017**, *8*, 7025−7030.
(45) Yu, Z.; Sun, Q.; Pan, W.; Li, N.; Tang, B. *ACS Nano* **2015**, *9*, 11064−11074.
(46) Huang, Y.; Yu, F.; Wang, J.; Chen, L. *Anal. Chem.* **2016**, *88*, 4122−4129.
(47) Huang, H.; Dong, F.; Tian, Y. *Anal. Chem.* **2016**, *88*, 12294−12302.
(48) Zhang, W.; Wang, X.; Li, P.; Xiao, H.; Zhang, W.; Wang, H.; Tang, B. *Anal. Chem.* **2017**, *89*, 6840−6845.
(49) Yu, F.; Gao, M.; Li, M.; Chen, L. *Biomaterials* **2015**, *63*, 93−101.
(50) Yang, L.; Chen, Y.; Yu, Z.; Pan, W.; Wang, H.; Li, N.; Tang, B. *ACS Appl. Mater. Interfaces* **2017**, *9*, 27512−27521.
(51) Würth, C.; Grabolle, M.; Pauli, J.; Spieles, M.; Resch-Genger, U. *Nat. Protoc.* **2013**, *8*, 1535−1550.
(52) Xiao, H.; Li, P.; Hu, X.; Shi, X.; Zhang, W.; Tang, B. *Chem. Sci.* **2016**, *7*, 6153−6159.
(53) Xu, H.; Aylott, J. W.; Kopelman, R.; Miller, T. J.; Philbert, M. A. *Anal. Chem.* **2001**, *73*, 4124−4133.
(54) Jung, S. K.; Gorski, W.; Aspinwall, C. A.; Kauri, L. M.; Kennedy, R. T. *Anal. Chem.* **1999**, *71*, 3642−3649.
(55) Koo, Y. E. L.; Cao, Y.; Kopelman, R.; Koo, S. M.; Brasuel, M.; Philbert, M. A. *Anal. Chem.* **2004**, *76*, 2498−2505.
(56) Younce, C. W.; Wang, K.; Kolattukudy, P. E. *Cardiovasc. Res.* **2010**, *87*, 665−674.
(57) Malhotra, J. D.; Kaufman, R. J. *Antioxid. Redox Signaling* **2007**, *9*, 2277−2294.
(58) Nakagawa, T.; Zhu, H.; Morishima, N.; Li, E.; Xu, J.; Yankner, B. A.; Yuan, J. *Nature* **2000**, *403*, 98−103.
(59) Yoshida, H.; Matsui, T.; Yamamoto, A.; Okada, T.; Mori, K. *Cell* **2001**, *107*, 881−891.
(60) Burkart, V.; Wang, Z. Q.; Radons, J.; Heller, B.; Herceg, Z.; Stingl, L.; Wagner, E. F.; Kolb, H. *Nat. Med.* **1999**, *5*, 314−319.
(61) Tang, Y.; Kong, X.; Xu, A.; Dong, B.; Lin, W. *Angew. Chem., Int. Ed.* **2016**, *55*, 3356−3359.
(62) Dai, Z. R.; Ge, G. B.; Feng, L.; Ning, J.; Hu, L. H.; Jin, Q.; Wang, D. D.; Lv, X.; Dou, T. Y.; Cui, J. N.; Yang, L. *J. Am. Chem. Soc.* **2015**, *137*, 14488−14495.

DOI: 10.1021/acs.analchem.7b05440
Anal. Chem. 2018, 90, 6081−6088